J. Fluid Mech. (1987), *vol.* 180, *pp.* 495–514
Printed in Great Britain

Creeping flow in two-dimensional channels

By C. POZRIKIDIS
Research Laboratories, Eastman Kodak Company, Rochester, NY 14650, USA

(Received 25 September 1986)

Creeping flow in two-dimensional periodic channels of arbitrary geometry is considered. The problem is formulated using the boundary-integral method for Stokes flow, presently adapted for periodic flows with special geometrical characteristics. Numerical calculations for steady flow in channels constricted by a plane and a sinusoidal wall are performed. Detailed streamline patterns are presented and criteria for flow reversal are established. It is shown that for narrow channels the mechanism driving the flow has a strong effect on the structure of the flow. The results are discussed with reference to lubrication, coating and molecular–convective processes.

1. Introduction

Flow in channels is encountered in diverse areas of fluid mechanics. The literature contains a large number of studies for a variety of flow conditions, corresponding to different physical situations.

Steady flows between two flexible or solid bodies in relative motion are often studied with reference to lubrication or coating processes (Langlois 1964). The two bodies are kept separated by strong pressure forces generated by the flow. In these processes it is of interest to determine how irregularities of the body surfaces affect the ratio of the friction force to weight of the bodies, and the flow rate. Pressure-driven flow in narrow channels with sudden expansions is important in the extrusion and coating of thin liquid films. The expansions dampen three-dimensional fluid motions causing product non-uniformities. In these applications it is important to design the channels to avoid low wall shear stress and onset of recirculating fluid regions. These may lead to particle or bubble entrapment, increased residence times, and build-up of chemical reactants. The above two examples demonstrate the importance of flows in corrugated channels for specific industrial processes. From a fundamental standpoint, these flows provide useful information for flows in complex media such as packed bed reactors and porous rocks. The analysis provides relationships for the flow properties as functions of the macroscopic material characteristics (Taylor 1971; Deiber & Schowalter 1979).

Unsteady flows are also studied with reference to various physical systems. In a simple class of flows, the motion is due to the steady propagation of waves along the flexible walls of a channel. Examples in this class include the locomotion of microscopic organisms, peristaltic pumping of sensitive or corrosive fluids, physiological flows in the human body (Pozrikidis 1987), and the generation of water waves by wind (Caponi *et al.* 1982). A second class of flows includes oscillatory flows over wavy surfaces. Onset of steady streaming motion, and periodic formation and expansion of eddies are two interesting phenomena associated with these flows (Hall 1974; Sobey 1983).

Apart from their importance in various natural and industrial systems, flows in corrugated channels are of pure fundamental interest; they constitute convenient prototypes for studying the mechanisms of viscous flow under different flow conditions. Similar systems consisting of walls with cavities, two intersecting planes, two cylinders, and a plane and a cylinder have been employed by previous authors (Hasimoto & Sano 1980). As an example, Jeffrey & Sherwood (1980) studied shear flow over a stationary cylinder tangent to a moving wall and established criteria for eddy formation at the points of contact.

We saw that there is a wide variety of applications involving flow in corrugated channels. To study different flow conditions, various methods have been employed. A common approach is to assume small wall corrugations, small channel widths, and very small or very large Reynolds numbers, and to write perturbation expansions in these variables. To consider the more realistic cases of finite amplitudes, numerical methods have been employed. These include finite difference, finite element, and spectral solutions, usually at intermediate and low Reynolds numbers. As expected, these methods are most effective for relatively simple flow geometries. The goal of the present article is to provide a detailed numerical investigation of flow in two-dimensional channels, in the limit of creeping motion. Emphasis will be placed on the fundamental description of the flow as well as on the application of the results to specific engineering processes.

The analysis is based on the boundary integral method for two-dimensional Stokes flow, presently extended to two-dimensional periodic flows with special geometrical features. The basic strength of the method is the simplicity of the required numerical procedure, allowing an accurate, detailed, and extended investigation.

In §§2 and 3 we present the mathematical formulation and develop the numerical procedure. In §4 we discuss shear and pressure driven flow in periodic channels constricted by a plane and a sinusoidal wall.

2. Mathematical formulation

We consider slow motion of a Newtonian fluid in a two-dimensional domain which may be bounded by a number of fluid, solid, and free surfaces or may extend to infinity. At low Reynolds numbers the flow is governed by the Stokes equation and the continuity equation

$$\frac{\partial \sigma_{ij}}{\partial x_i} = 0, \tag{1}$$

$$\frac{\partial u_i}{\partial x_i} = 0, \tag{2}$$

respectively, where σ_{ij} is the stress tensor, $\sigma_{ij} = -\delta_{ij} P + \mu(\partial u_i/\partial x_j + \partial u_j/\partial x_i)$. These equations constitute a system of linear, elliptic, partial differential equations, whose solution may be conveniently expressed as an integral over the flow boundary (Higdon 1985). The result for points on the flow boundary is

$$u_j(\boldsymbol{x}) = \frac{1}{2\pi\mu} \int [S_{ij}(\boldsymbol{x}, \boldsymbol{x}') f_i(\boldsymbol{x}') - T_{ijk}(\boldsymbol{x}, \boldsymbol{x}')\, u_i(\boldsymbol{x}')\, \eta_k] \, ds(\boldsymbol{x}'). \tag{3}$$

For points in the interior of the flow, the factor $2\pi\mu$ in the denominator should be replaced by $4\pi\mu$. In the above equation, $f_i = \sigma_{ik}\eta_k$ is the boundary force, and η_k is

the unit vector normal to the boundary pointing *into* the fluid. When the flow extends to infinity, the boundary is assumed to include a circle or part of a circle of infinite radius. In this case, care must be taken for the convergence of the integral.

The tensor S_{ij} represents a singular fundamental solution to Stokes equation with a logarithmic singularity. The velocity, pressure, and stress field associated with this solution may be written in the form

$$\left.\begin{aligned} u_i(x') &= \frac{1}{4\pi\mu} S_{ij}(x, x')\, a_j, \\ P(x') &= \frac{1}{4\pi\mu} P_j(x, x')\, a_j, \\ \sigma_{ik}(x') &= \frac{1}{4\pi\mu} T_{ijk}(x, x')\, a_j, \end{aligned}\right\} \tag{4}$$

where $T_{ijk} \sim 1/|x'-x|$ as $|x'-x| \to 0$, and a_j is an arbitrary constant. T_{ijk} is the stress tensor corresponding to S_{ij}, defined as $T_{ijk} = -\delta_{ik} P_j + \mu(\partial S_{ij}/\partial x'_k + \partial S_{kj}/\partial x'_i)$. Using the divergence theorem, one may write (3) in an alternative form,

$$u_j(x) = \frac{1}{2\pi\mu} \int \left[S_{ij}(x, x') \left(-P\eta_i + \mu \frac{\partial u_i}{\partial n} \right) - \left(-P_j \eta_i + \mu \frac{\partial S_{ij}}{\partial n} \right) u_i(x') \right] \mathrm{d}s(x'), \tag{5}$$

where $\partial/\partial n$ denotes differentiation normal to the boundary in the direction of the fluid (Happel & Brenner 1965, p. 81). Equation (3) is a singular Fredholm equation of the first kind for the boundary force, and of the second kind for the boundary velocity. Appropriate forms of this equation for interior or exterior flows are given by Higdon (1985) and by Lee & Leal (1986).

The choice of the fundamental solution S_{ij} is important for the efficient implementation of the solution scheme. Therefore, we would like to discuss it in some detail.

The simplest choice is the two-dimensional Stokeslet

$$\left.\begin{aligned} S^{\mathrm{ST}}_{ij}(\hat{x}) &= \delta_{ij} \ln r - \frac{\hat{x}_i \hat{x}_j}{r^2}, \\ P^{\mathrm{ST}}_j(\hat{x}) &= -2\mu \frac{\hat{x}_j}{r^2}, \\ T^{\mathrm{ST}}_{ijk}(\hat{x}) &= 4\mu \frac{\hat{x}_i \hat{x}_j \hat{x}_k}{r^4}, \end{aligned}\right\} \tag{6}$$

where $\hat{x} = x' - x$, and $r = |\hat{x}|$ (Ladyzhenskaya 1969, p. 67). In this case, (4) and (6) yield the flow at the point x', associated with a point force of strength $|a|$ located at x, pointing in the $-a$-direction.

Other fundamental solutions may be employed to exploit specific geometrical features. Blake (1971) proposed a fundamental solution which preserves zero velocity along a plane, placed at $y = w$. This may be derived from Lorentz formula (see Happel & Brenner 1965, p. 87), and is composed of a Stokeslet and a collection of image Stokeslets, Stokes-Doublets, and potential source-Doublets

$$\boldsymbol{S}^{\mathrm{W}}(x, x') = \boldsymbol{S}^{\mathrm{ST}}(\hat{x}) - \boldsymbol{S}^{\mathrm{ST}}(\tilde{x}) - 2(y-w)\,\boldsymbol{D}(\tilde{x}) - 2(y-w)^2\,\boldsymbol{P}(\tilde{x}), \tag{7}$$

where $\tilde{\boldsymbol{x}} = (\tilde{x}, \tilde{y}) = (x'-x, y'+y-2w)$, and values of the indices 1 and 2 indicate the x- and y-direction respectively. The matrices $\boldsymbol{D}$ and $\boldsymbol{P}$ are defined as

$$\left.\begin{aligned} \boldsymbol{D} &= \frac{\partial}{\partial \tilde{x}} \begin{bmatrix} -\dfrac{\tilde{x}\tilde{y}}{\rho^2} & \ln\rho - \dfrac{\tilde{x}^2}{\rho^2} \\ \ln\rho - \dfrac{\tilde{y}^2}{\rho^2} & -\dfrac{\tilde{x}\tilde{y}}{\rho^2} \end{bmatrix}, \quad \text{Stokes-Doublets} \\ \boldsymbol{P} &= \begin{bmatrix} \dfrac{\partial}{\partial \tilde{x}}\left(\dfrac{\tilde{x}}{\rho^2}\right) & -\dfrac{\partial}{\partial \tilde{y}}\left(\dfrac{\tilde{x}}{\rho^2}\right) \\ \dfrac{\partial}{\partial \tilde{x}}\left(\dfrac{\tilde{y}}{\rho^2}\right) & -\dfrac{\partial}{\partial \tilde{y}}\left(\dfrac{\tilde{y}}{\rho^2}\right) \end{bmatrix}, \quad \text{source-Doublets} \end{aligned}\right\} \tag{8}$$

with $\rho = |\tilde{\boldsymbol{x}}|$. This fundamental solution is useful in problems involving the motion of bodies near a plane wall.

For a flow that is symmetric with respect to a plane at $y = w$, it is useful to introduce a fundamental solution that yields zero velocity normal to this plane at $y' = w$,

$$S_{ij}^{\mathrm{SW}} = S_{ij}^{\mathrm{ST}}(\hat{\boldsymbol{x}}) + (-1)^{j+1} S_{ij}^{\mathrm{ST}}(\tilde{\boldsymbol{x}}), \tag{9}$$

where again $i, j = 1, 2$ indicate the x- and y-direction respectively. This solution is schematically illustrated in figure 1 (a). Similarly, for a flow which is symmetric with respect to a point, we introduce the solution $\boldsymbol{S}^{\mathrm{SP}}$, illustrated in figure 1 (b).

For flows that are periodic in the x-direction, it is convenient to introduce a periodic fundamental solution representing an array of point forces along the x-axis. The velocity and stress tensors may be expressed in closed form by summing (5)

$$\left.\begin{aligned} \boldsymbol{S}^{\mathrm{STP}}(\hat{\boldsymbol{x}}) &= \begin{bmatrix} A + k\hat{y}A_y - 1 & -k\hat{y}A_x \\ -k\hat{y}A_x & A - k\hat{y}A_y \end{bmatrix}, \\ P_i^{\mathrm{STP}}(\hat{\boldsymbol{x}}) &= -2\mu A_{x_i}, \\ T_{xxx}^{\mathrm{STP}} &= 2\mu \operatorname{div}(A, k\hat{y}A_x), \\ T_{xxy}^{\mathrm{STP}} &= 2\mu \operatorname{div}(-k\hat{y}A_x, A), \\ T_{xyy}^{\mathrm{STP}} &= 2\mu \operatorname{div}(A, -k\hat{y}A_x), \\ T_{yyy}^{\mathrm{STP}} &= 2\mu \operatorname{div}(k\hat{y}A_x, A), \\ T_{ijk}^{\mathrm{STP}} &= T_{kij}^{\mathrm{STP}} = T_{jki}^{\mathrm{STP}}, \end{aligned}\right\} \tag{10}$$

with

$$A = \tfrac{1}{2}\ln[2(\cosh(k\hat{y}) - \cos(k\hat{x}))], \tag{11}$$

where λ is the separation between the point forces, $k = 2\pi/\lambda$ is the wavenumber, and A_x, A_y, indicate derivatives of A with respect to $k\hat{x}$ and $k\hat{y}$ respectively. One may readily verify that as $|\hat{\boldsymbol{x}}| \to 0$, this solution behaves like a Stokeslet. Similarly, for semi-infinite periodic flows that are bounded by a plane wall or are symmetric with respect to a plane or a point, we introduce the periodic versions of $\boldsymbol{S}^{\mathrm{W}}$, $\boldsymbol{S}^{\mathrm{SW}}$, and $\boldsymbol{S}^{\mathrm{SP}}$, denoted as $\boldsymbol{S}^{\mathrm{WP}}$, $\boldsymbol{S}^{\mathrm{SWP}}$, and $\boldsymbol{S}^{\mathrm{SPP}}$ respectively. These may be expressed in closed form by direct summation.

The simplification owing to the use of the appropriate fundamental solution may

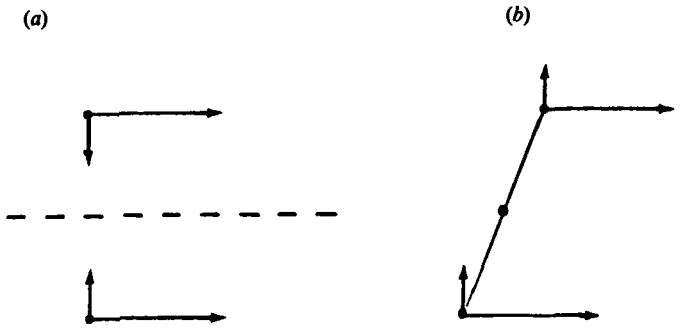

FIGURE 1. Fundamental solution of Stokes equation for a flow symmetric with respect (*a*) to a plane and (*b*) to a point; the vectors represent Stokeslets.

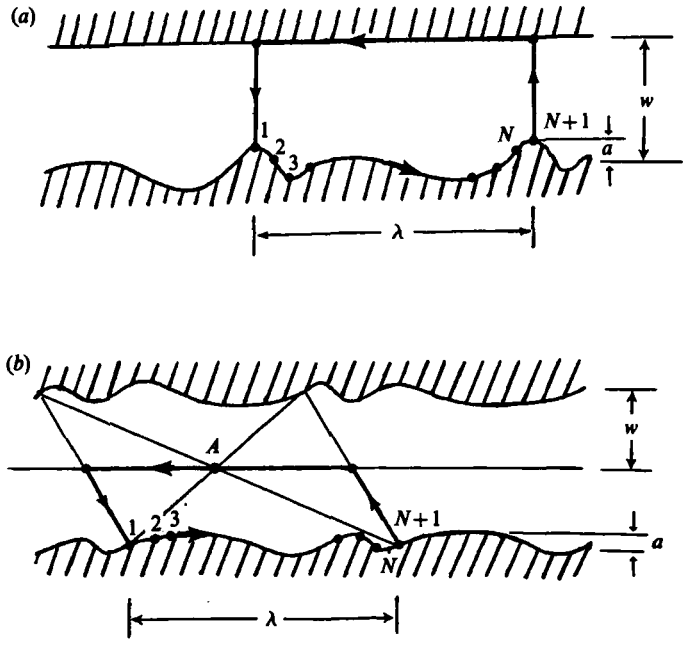

FIGURE 2. Periodic flow in two-dimensional channels; (*a*) flow constricted by a plane and a corrugated wall, (*b*) flow constricted by two walls that are symmetric with respect to the point A; w is the channel width and a is the amplitude of the corrugations.

be illustrated by considering flow in the channels shown in figure 2. In the first case (figure 2*a*) we use the fundamental solution $\mathbf{S}^{\mathrm{WP}}$ and integrate (3) along the indicated contour enclosing one fluid period. For zero net pressure drop, the integrals along the two vertical segments cancel, whereas the integral along the plane wall is equal to twice the velocity of this wall. Similarly for flow in the channel shown in figure 2(*b*), we use the solution $\mathbf{S}^{\mathrm{SPP}}$, and integrate (3) along the indicated contour. Again, for zero net pressure drop, the contribution from the straight segments vanishes. Thus, in both cases, the velocity is expressed simply as an integral over one period of the wavy wall. Use of the appropriate fundamental solution for the corresponding flow geometry will be implicit throughout the following discussion.

3. Numerical procedure

In this section we develop a numerical method for solving (3) for the boundary force $f_i(\boldsymbol{x}')$ given the boundary velocity $u_i(\boldsymbol{x}')$, with particular reference to the channel flows depicted in figure 2. It is important to note that the boundary velocity may be specified either as a total or as a disturbance quantity. When the flow is driven by the motion of the boundaries, it is convenient to consider the total velocity; when it is driven by an imposed mean pressure gradient or by the presence of body forces, it is convenient to consider the disturbance flow owing to the boundary deviation from a known reference state.

Our numerical procedure employs a collocation method, similar to that suggested by Higdon (1985). First, we identify a set of $N+1$ points along one period of the appropriate channel boundary (figure 2). The boundary shape is approximated as a polygonal line composed of N straight segments connecting these points. The boundary velocity is approximated as a linear function, whereas the boundary force is approximated as a constant function f_i^n, over the nth segment. Next, we apply (3) at the middle of each segment $\boldsymbol{x}_m$, to obtain the following system of linear algebraic equations for f_i^n,

$$u_j(\boldsymbol{x}_m) + \sum_{n=1}^{N} B_j^n(\boldsymbol{x}_m) = \sum_{n=1}^{N} A_{ij}^n(\boldsymbol{x}_m) f_i^n, \tag{12}$$

where

$$\left.\begin{aligned} A_{ij}^n(\boldsymbol{x}_m) &= \frac{1}{2\pi\mu}\int_{S_n} S_{ij}(\boldsymbol{x}_m, \boldsymbol{x}')\,\mathrm{d}s(\boldsymbol{x}'), \\ B_j^n(\boldsymbol{x}_m) &= \frac{1}{2\pi\mu}\int_{S_n} T_{ijk}(\boldsymbol{x}_m, \boldsymbol{x}')\,u_i(\boldsymbol{x}')\,\eta_k\,\mathrm{d}s(\boldsymbol{x}'). \end{aligned}\right\} \tag{13}$$

S_n denotes integration over the nth segment. The singular integrals in (13) may be evaluated numerically by subtracting and adding the Stokeslet,

$$\left.\begin{aligned} \int S_{ij}\,\mathrm{d}s &= \int (S_{ij} - S_{ij}^{\mathrm{ST}})\,\mathrm{d}s + \int S_{ij}^{\mathrm{ST}}\,\mathrm{d}s, \\ \int T_{ijk}\,u_i\,n_k\,\mathrm{d}s &= \int (T_{ijk} - T_{ijk}^{\mathrm{ST}})\,u_i\,n_k\,\mathrm{d}s + \int T_{ijn}^{\mathrm{ST}}\,u_i\,n_k\,\mathrm{d}s. \end{aligned}\right\} \tag{14}$$

The second integrals in the right-hand side of (14), associated with the Stokeslet, are evaluated analytically over each segment. Finally, the linear algebraic system (12) is solved using standard Gauss elimination.

The efficiency of the above method was tested by solving for simple shear flow in infinite fluid, considering as a control volume the channel shown in figure 2(*a*) for different cell widths w/λ and wave amplitudes a/λ; for this flow, the method yields the exact solution. Indeed, our results were accurate up to the fifteenth decimal place, limited by the computer round-off error.

Higdon (1985) showed that the relative error in the above approximation is of order δ^2, where δ is the segment length. Specifically, the relative error in evaluating the integrals in (12), associated with the polygonal boundary approximation, is of order $\delta^2 k^2$, where k is the local boundary curvature of order one for smooth boundaries. Further, the relative error owing to the linear approximation of the boundary velocities and the stepwise approximation of the boundary forces is of order δ^2. This yields a consistent, order δ^2 total relative error.

Knowing the behaviour of the relative error is beneficial in obtaining high-accuracy

results while using a moderate number of points. We use successive Romberg extrapolation from primary runs with $n = 20, 40, 80$, and occasionally 160, to increase the accuracy up to δ^8. The observed fast convergence confirms the error analysis and validates our procedure.

4. Results and discussion

We consider steady flow in a periodic channel constricted by a plane wall at $y = w$, and a sinusoidal wall at $y = -a\cos(kx)$. This flow may be driven by two independent mechanisms: the steady, horizontal translation of the plane wall, and the presence of a mean pressure gradient $G = -\mathrm{d}P/\mathrm{d}x$. In the trivial case of zero wave amplitude, these reduce to plane Couette and plane Poiseuille flow, respectively. The two cases will be considered independently with a linear superposition possible owing to the linearity of Stokes equation. To clarify the computational procedure, we note that in the shear-driven case we calculate the total flow, whereas in the pressure-driven case we calculate the disturbance flow owing to the amplitude of the wavy wall.

4.1. '*Shear-driven flow*'

First, we consider flow in narrow channels, taking as a typical example the case $w/\lambda = 0.100$. Figure 3(*a*) illustrates the changes in the streamline pattern as the wave amplitude a/λ is increased from 0.025 to 0.090. When $a/\lambda = 0.025$, the streamlines are smooth, adjusting to the curvature of the wavy wall. Doubling the amplitude of the wave causes a strong expansion of the fluid at the trough of the wavy wall, leading to development of adverse pressure gradients and to flow reversal. The developed eddies occupy almost the entire space of the sinusoidal corrugations, leaving only a narrow gap for longitudinal fluid transport. As the wave amplitude becomes very close to the channel width the channel reduces into a series of independent cells, and the flow within each cell is essentially flow in a cavity driven by a moving lid (Pan & Acrivos 1967). The structure of the flow may be better visualized by considering the velocity profiles along the centre line $x = 0$ (figure 4*a*). We observe an almost linear profile for small amplitudes, and a parabolic profile for large amplitudes, with significnt regions of recirculating flow.

The above calculations demonstrate the onset of reversed-flow regions, when the wave amplitude exceeds a critical value. Flow reversal is indicated by a change in sign of the vorticity or the shear stress along the wavy wall. The distribution of shear stress along the wavy wall for the three flows discussed above is presented in figure 5(*a*). As the wave amplitude is increased, the shear stress at the trough decreases rapidly, and touches the zero axis when $a/\lambda = 0.030$. This defines the critical wave amplitude for flow reversal.

The magnitude of the wall shear stress is important in applications involving molecular–convective processes at high Prandtl or Schmidt numbers (Higdon 1985). The pronounced maximum at the crest of the wavy wall indicates increased local transport, which may be responsible for a number of effects. For instance, a dissolving wavy wall will tend to level out under the high shear rate at the crests. Similarly, a chemical reaction between the wall material and the fluid, with deposition of products, will cause a fast increase in the wall amplitude and possible clogging of the channel.

It is interesting to consider in some detail the structure of the developed viscous eddies. We saw that the size of these eddies is a function of wave amplitude. To illustrate this clearly, we consider the eddy height, h, defined as the vertical distance

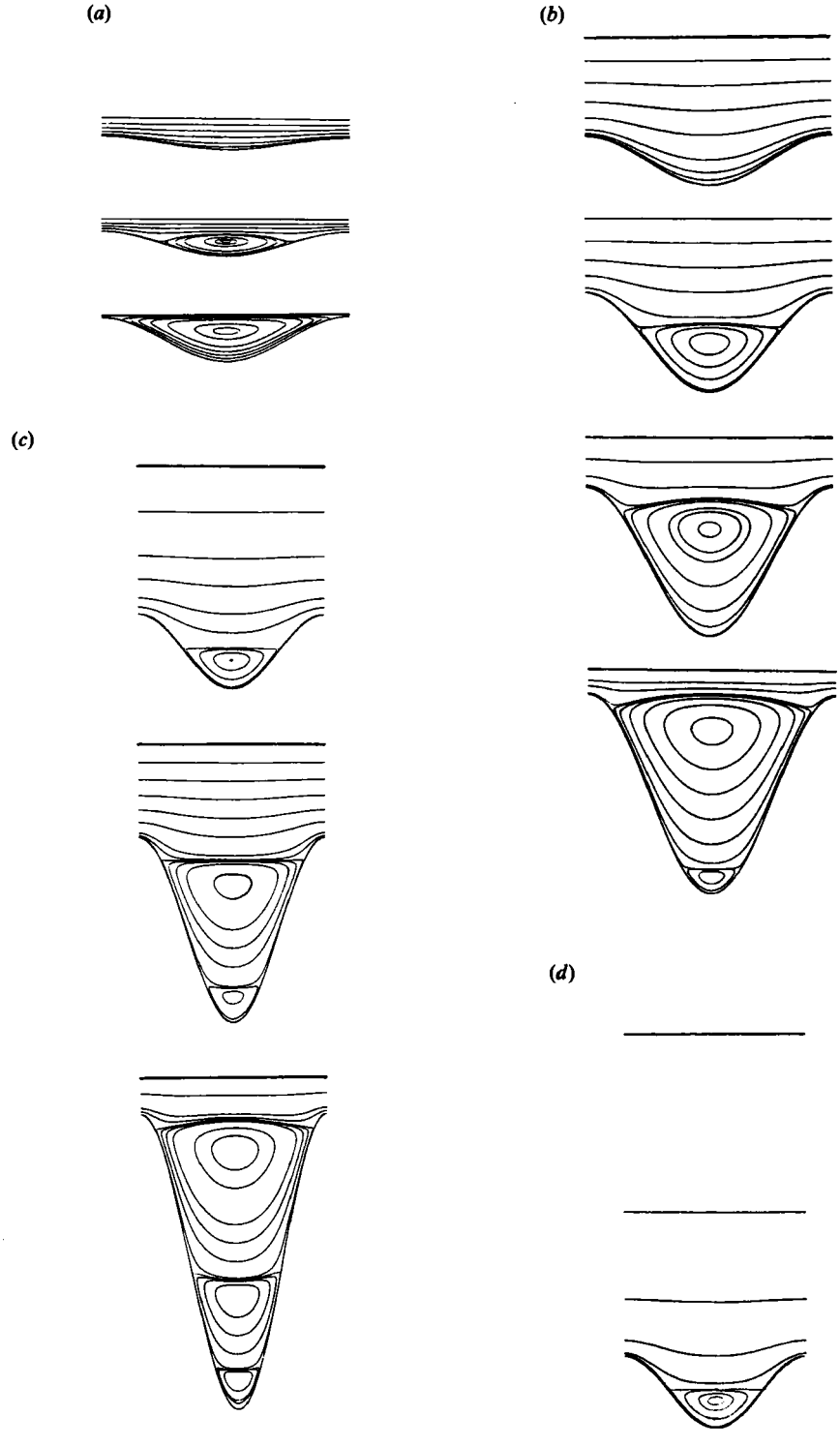

FIGURE 3. Streamline patterns for Couette flow in channels of (a) width $w/\lambda = 0.100$, and wave amplitude $a/\lambda = 0.025, 0.050, 0.090$; (b) $w/\lambda = 0.500$, and $a/\lambda = 0.100, 0.200, 0.300, 0.400$; (c) $w/\lambda = 1.000$, and $a/\lambda = 0.200, 0.500, 0.800$; (d) $w/\lambda = 2.000$, and $a/\lambda = 0.200$.

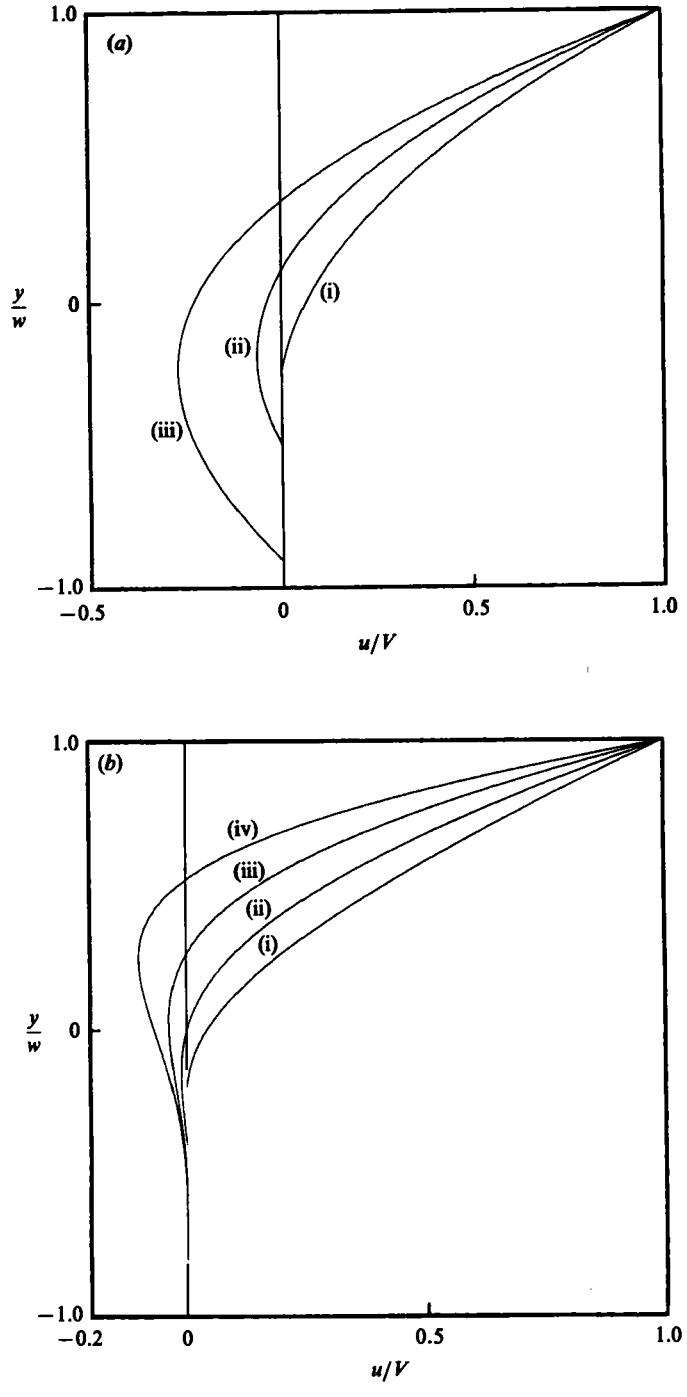

FIGURE 4. Velocity profile along the vertical at $x = 0$, for Couette flow in a channel of (*a*) width $w/\lambda = 0.100$ and wave amplitude (i) $a/\lambda = 0.025$, (ii) $a/\lambda = 0.050$, (iii) $a/\lambda = 0.090$; (*b*) $w/\lambda = 0.500$, and (i) $a/\lambda = 0.100$, (ii) $a/\lambda = 0.200$, (iii) $a/\lambda = 0.300$, (iv) $a/\lambda = 0.400$.

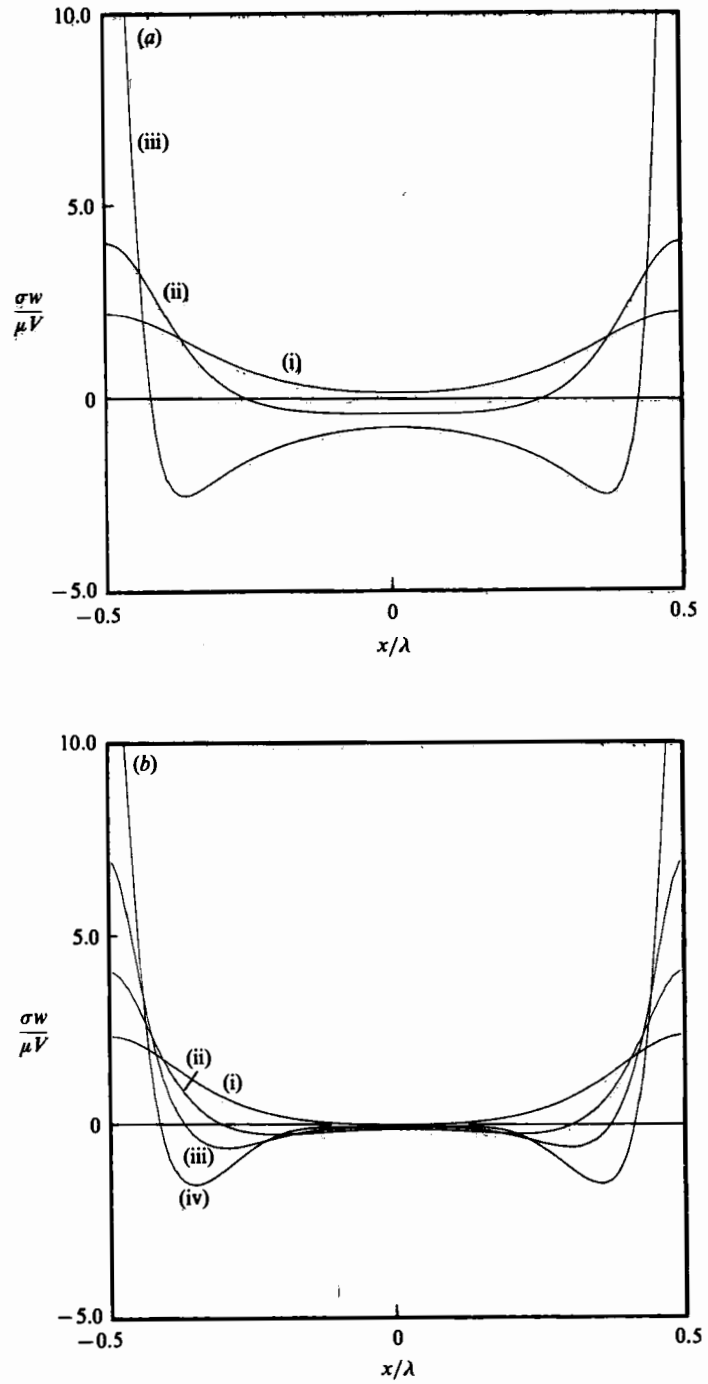

FIGURE 5. Shear stress distribution along the wavy wall for Couette flow in a channel of (*a*) width $w/\lambda = 0.100$ and wave amplitude (i) $a/\lambda = 0.025$, (ii) $a/\lambda = 0.050$, (iii) $a/\lambda = 0.090$; (*b*) $w/\lambda = 0.500$, and (i) $a/\lambda = 0.100$, (ii) $a/\lambda = 0.200$, (iii) $a/\lambda = 0.300$, (iv) $a/\lambda = 0.400$.

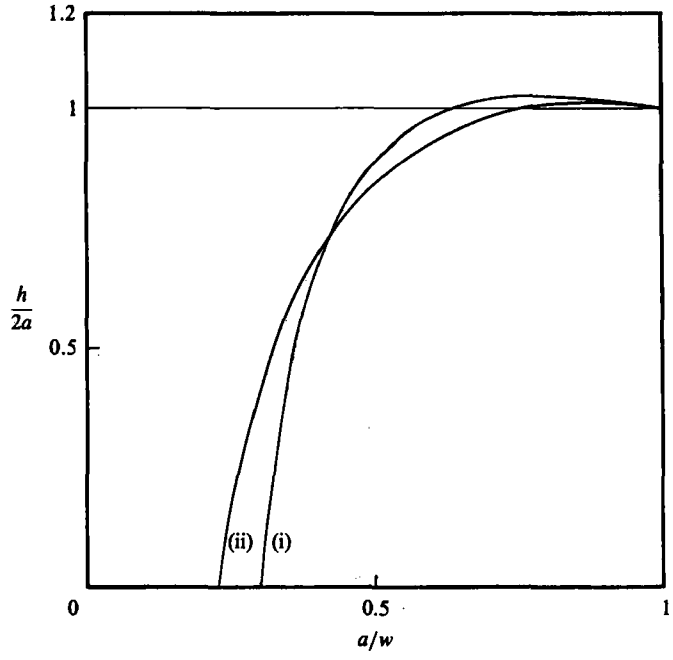

FIGURE 6. Eddy size at trough as a function of wave amplitude, for Couette flow in a channel of (i) $w/\lambda = 0.100$, (ii) $w/\lambda = 0.500$

between the dividing streamline enclosing these eddies and the wavy wall at $x = 0$. In figure 6, we plot the reduced eddy height $h/2a$ as a function of wave amplitude a/w. This is equal to zero for non-reversing flow, $a/w < 0.301$, but then, it increases rapidly, reaches a maximum, and finally, as $a/w \to 1$, it tends to unity. The maximum height, $h/2a$, is greater than one, indicating that eddies may protrude above the crests of the wavy wall. In contrast, the strength of the eddies, expressd by the x-velocity on the dividing streamline at $x = 0$, increases in a monotonic, smooth fashion. These results indicate that near the critical conditions for eddy formation, the flow is very sensitive to small changes in the boundary geometry. As a consequence, the fabrication of channels should be monitored very accurately to avoid large regions of recirculating fluid.

Proceeding to wider channels, we concentrate on the case $w/\lambda = 0.500$ (figure 3*b*). As previously, for small wave amplitudes, the streamlines follow the curvature of the sinusoidal wall, whereas for larger amplitudes flow reversal occurs. In the present case, as the wave amplitude becomes close to the channel width, secondary eddies develop at the trough of the corrugations. The velocity profile at $x = 0$ for each of the above patterns is presented in figure 4*b*. We note the weak fluid motion at the trough of the corrugations for large wave amplitudes. The shear stress distribution along the wavy wall is shown in figure 5*b*. As in the narrow channel case, the shear stress reaches a maximum at the wave crests and drops to very low values along the rest of the wavy wall. The curve for $a/\lambda = 0.400$ crosses the zero axis twice, indicating the presence of secondary eddies. The height of the primary eddies shows behaviour similar to that for narrow channels (figure 6).

Onset of secondary eddies inside deep corrugations is predicted by a number of previous studies (Higdon 1985). In particular, Moffatt (1964) predicted the develop-

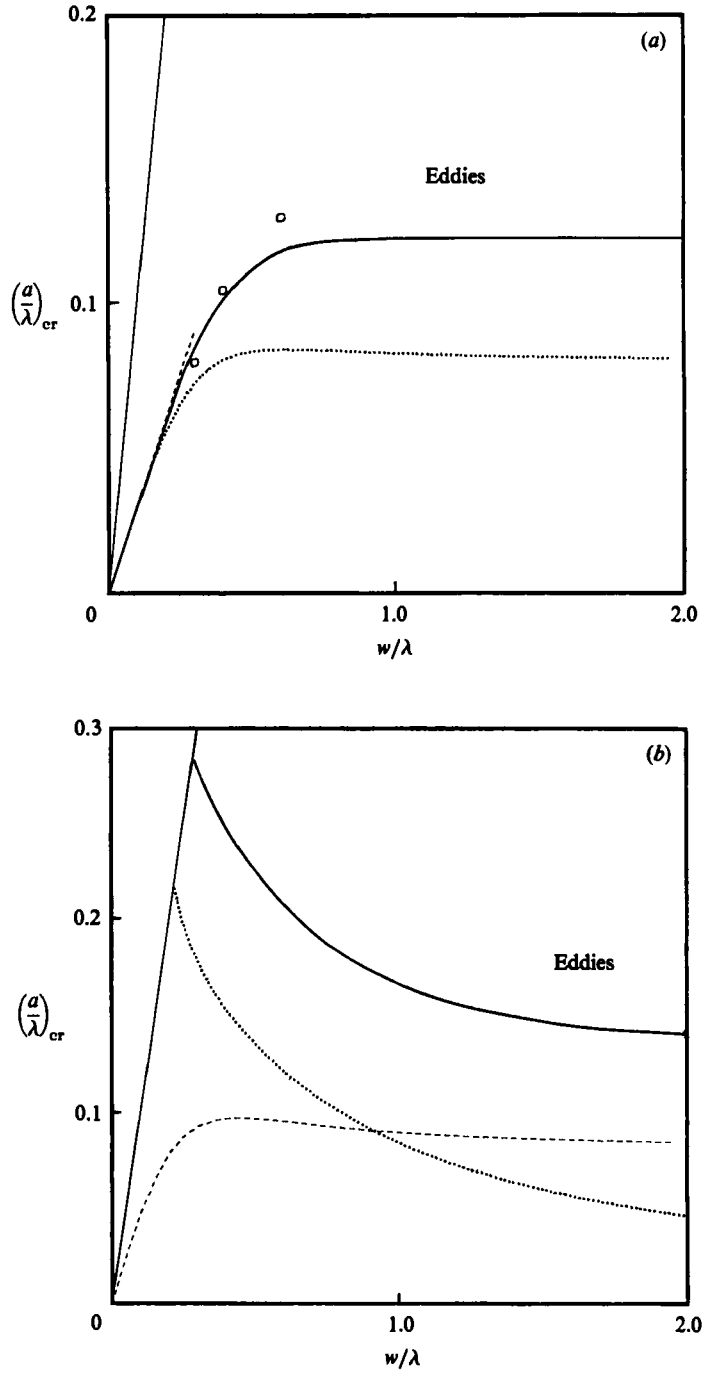

FIGURE 7. Critical wave amplitude for flow separation as a function of channel width for (*a*) Couette and (*b*) Poiseuille flow. The straight solid line defines the physical boundary, $a < w$. In (*a*) dashed line shows predictions of first-order perturbation theory for small w/λ; the dotted line shows predictions of second-order perturbation theory for small a/λ; circles show experimental results by Munson *et al.* (1985). In (*b*) dotted line shows predictions of first-order perturbation theory for small w/λ; the dashed line shows predictions of second-order perturbation theory for small a/λ.

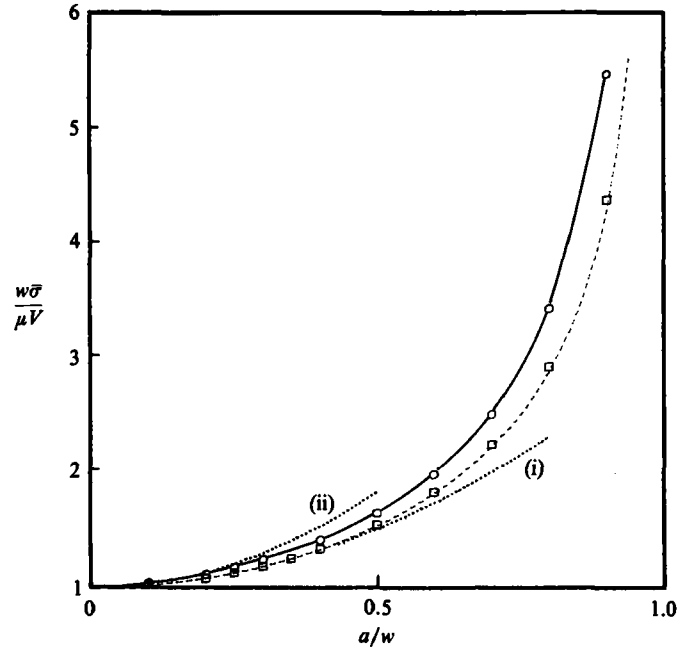

FIGURE 8. Drag force on the plane wall as a function of wave amplitude for Couette flow in a channel of (i) □, $w/\lambda = 0.100$, (ii) ○, $w/\lambda = 0.500$. The dashed line shows predictions of first-order perturbation theory for small w/λ, and dotted lines predictions of second-order perturbation theory for small a/w.

ment of an infinite sequence of self-similar eddies at the corner between two stationary solid planes, for sufficiently small angles of inclination. It is of interest to examine whether the two eddies shown in the lower frame of figure 3(*b*) may be described by Moffatt's similarity solution. For this purpose, we evaluate their strength ratio equal to 922, and calculate the angle of inclination corresponding to this value according to Moffatt. This is equal to $\frac{2}{5}\pi$, very close to the angle formed by the tangents to the wavy wall at the lower points of separation. This demonstrates that the flow inside the corrugations tends to attain a self-similar state, even at moderate wave amplitudes. Thus, onset of eddies may be understood in terms of Moffatt's local analysis.

To show the behaviour for wider channels, we present streamline patterns for $w/\lambda = 1.000$ and 2.000 (figure 3*c*, *d*). The first demonstrates the onset of a series of alternating eddies for very deep corrugations in agreement with Moffatt (1964). The second is characteristic of simple shear flow over a wavy wall, recovered from our calculations for large w/a.

We saw that for every channel width w/λ there is a critical wall amplitude, $(a/\lambda)_{cr}$, for flow reversal. In figure 7(*a*), we plot $(a/\lambda)_{cr}$ as a function of w/λ, along with previous experimental results (Munson, Rangwella & Mann 1985), predictions of second-order perturbation theory for small amplitudes a/w (Appendix), and predictions of first-order perturbation theory for small channel widths w/λ (Hasegawa & Izuchi 1984). We observe a good agreement between the numerical and experimental predictions; the small differences are attributed to the cylindrical geometry used by the above authors. Perturbation expansions fail to predict flow reversal with reasonable accuracy, except for very narrow channels, and therefore, they are of

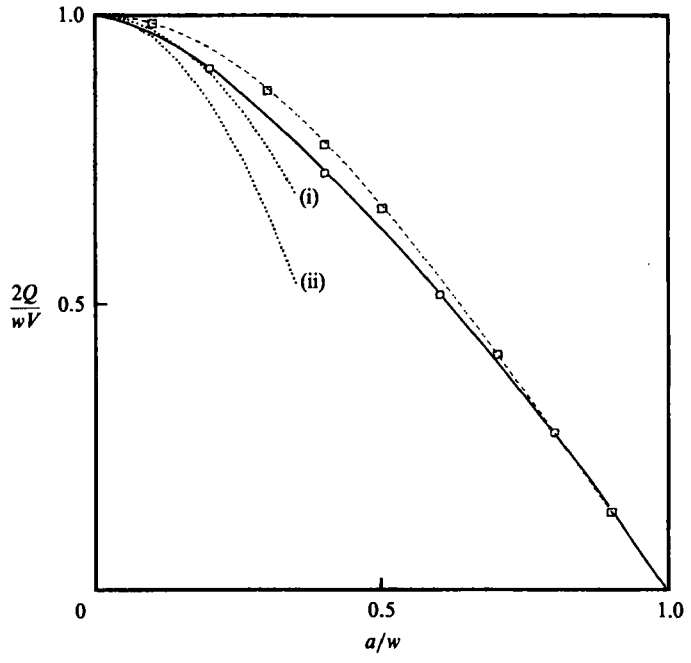

FIGURE 9. Flow rate as a function of wave amplitude for Couette flow in a channel of (i) □, $w/\lambda = 0.100$, (ii) ○, $w/\lambda = 0.500$. The dashed line shows predictions of first-order perturbation theory for small w/λ, and dotted lines predictions of second-order perturbation theory for small a/w.

limited practical interest. At large amplitudes, the incipient flow-reversal curve tends to an asymptotic value, characteristic of simple shear flow over a sinusoidal wall. Looking at figure 7 (a) from a different perspective, we consider the wave amplitude a/λ fixed, and vary the channel width w/λ. This indicates that eddies may be produced for any wave amplitude by sufficiently decreasing the channel width. Narrower channels cause stronger adverse pressure gradients, responsible for flow reversal.

Concluding this section, we would like to discuss the effect of the channel geometry on certain bulk properties of the flow, namely the drag force on the moving plane and the flow rate. The first is important in lubrication processes, whereas the second is important in coating or pumping operations. These are presented in figures 8 and 9, along with predictions of perturbation theories. Considering first the drag force, we note the parabolic increase for small a/v and the singular behaviour as a/w tends to unity. Perturbation analysis predicts that this singularity is of the order $w/(w-a)^{\frac{1}{2}}$, as compared with λ/w for zero wave amplitude (Hasegawa & Izuchi 1984). Thus, measuring the drag force may provide a potential method for estimating wall roughness. It is interesting to note that the drag force is approximately doubled when the wave amplitude becomes equal to half the channel width. Figure 9 shows that the flow rate decreases at a parabolic rate for small amplitudes, and at an almost linear rate for large amplitudes. It vanishes when the gap between the two walls becomes zero. The onset of eddies does not affect the drag force or the flow rate in any apparent fashion.

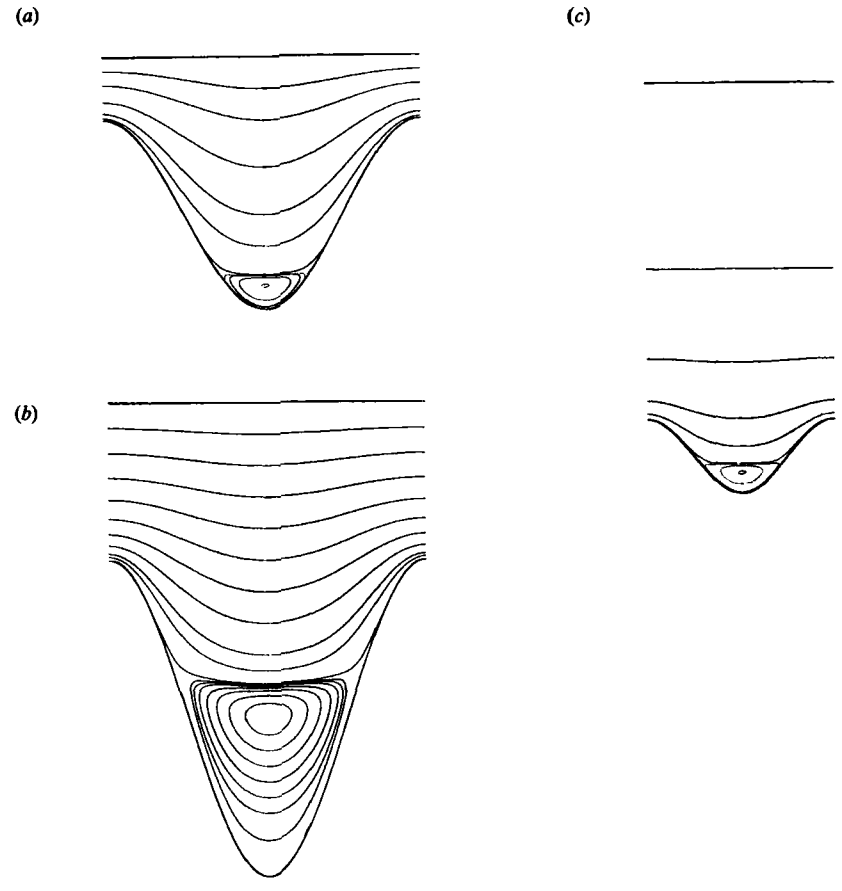

FIGURE 10. Streamline patterns for Poiseuille flow in a channel of (*a*) width $w/\lambda = 0.500$ and wave amplitude $a/\lambda = 0.300$; (*b*) $w/\lambda = 1.000$ and $a/\lambda = 0.500$; (*c*) $w/\lambda = 2.000$ and $a/\lambda = 0.200$.

4.2. *Pressure-driven flow*

In this section we consider flow driven by an imposed mean pressure gradient $G = -\mathrm{d}P/\mathrm{d}x$. We discuss our results with respect to those for shear-driven flow, indicating the differences between the two configurations. First, we note that for very wide channels, the structure of the flow in the vicinity of the wavy wall is independent of the type of flow. It may be substantially different for narrow channels, reflecting variations in the driving mechanism.

Our calculations show that in a narrow channel $w/\lambda = 0.100$, the streamlines adjust to the curvature of the wavy wall for any wave amplitude. This constitutes a fundamental difference from the shear-driven case for which the flow reverses when $a/\lambda = 0.030$. Physically, in the pressure-driven case, the imposed mean pressure gradient is able to defeat any developing local adverse pressure gradients.

Proceeding to wider channels, we consider a channel with $w/\lambda = 0.500$ and $a/\lambda = 0.300$, figure 10(*a*). A comparison with figure 3(*b*) (third frame) shows that in pressure-driven flow, the fluid is able to penetrate much deeper into the sinusoidal corrugations, causing a reduction in eddy size. Calculations for larger wave amplitudes show that the developing eddies never fill up the entire channel; there is always a substantial region of non-reversing flow attached to the plane wall. In the limit as

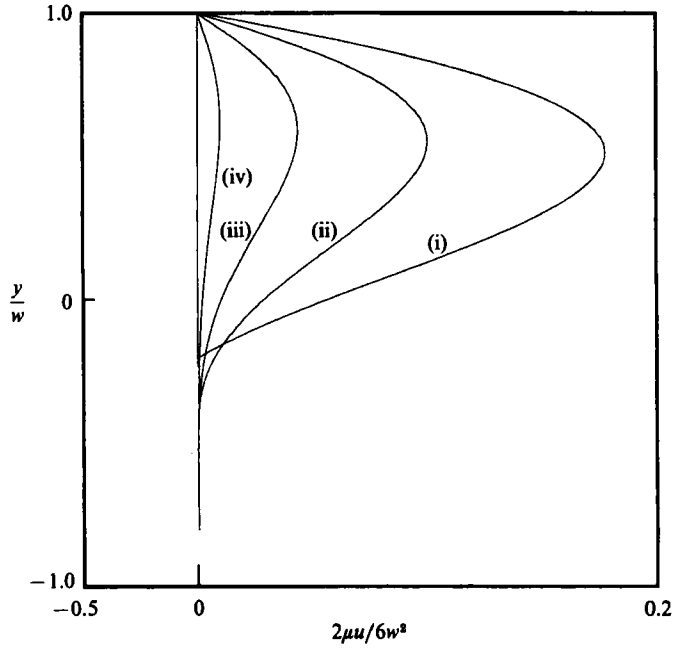

FIGURE 11. Velocity profile along the vertical at $x = 0$, for Poiseuille flow in a channel of $w/\lambda = 0.500$, and (i) $a/\lambda = 0.100$, (ii) $a/\lambda = 0.200$, (iii) $a/\lambda = 0.300$, (iv) $a/\lambda = 0.400$.

$a \to w$, the reduced eddy size $h/(2a)$ tends to 0.25, as opposed to unity for shear driven flow.

The above results demonstrate that the structure of the flow may be critically affected by the mechanism driving the flow. Velocity profiles at $x = 0$ for pressure-driven flow are presented in figure 11, and may be compared with those for shear-driven flow, figure 4(*b*). We notice the rapid decrease of the velocity with increasing wave amplitude. This is a result of our non-dimensionalization (with respect to the mean pressure gradient), and is attributed to the rapid increase in wall drag force, and therefore in flow rate, with increasing the wave amplitude. The strength of the eddies is substantially smaller than that for shear-driven flow, owing to the fact that in the present case, the eddies reside more deeply into the corrugations. Considering the shear stress distribution (figure 12), we note the pronounced maximum at the wave crests, familiar from shear-driven flow. However, now we observe a smoother decrease around the maximum, suggesting a milder effect on molecular–convective processes. The shear stress at the wave crest is a function of wave amplitude, reaching an extreme value approximately when $a/\lambda = 0.200$. This is expected, since for a specified pressure gradient, increasing a/λ, causes a local acceleration of the flow above the crests, simply for mass conservation, but also a reduction in the flow rate; the combined effect yields a maximum. Interpreting this behaviour, we conclude that for a specified pressure drop, there is an optimum wave amplitude for fastest convective transport.

Flow reversal in pressure driven flow may be understood by considering the individual mechanisms dominating different flow regions. For large wave amplitudes, the flow within the corrugations is dominated by the similarity solution of Moffatt (1964), describing an infinite sequence of eddies. On the other hand, as $a/w \to 1$, the

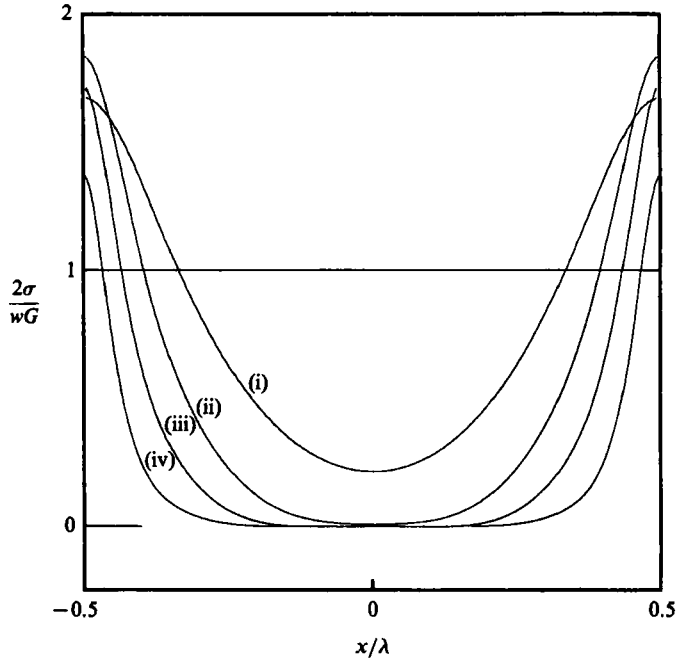

FIGURE 12. Shear stress distribution along the wavy wall for Poiseuille flow in a channel of $w/\lambda = 0.50$, and (i) $a/\lambda = 0.100$, (ii) $a/\lambda = 0.200$, (iii) $a/\lambda = 0.300$, (iv) $a/\lambda = 0.400$.

flow in the vicinity of the wave crests is dominated by the Jeffery–Hamel similarity solution (Fraenkel 1962). This describes flow in a wedge confined by two planes, with a point source or point sink at the apex. In the limit of zero Reynolds number, and when the wedge angle 2α is less than 1.43π, the velocity field in polar coordinates is given by the similarity solution

$$u_r = 2\frac{Q}{r}\frac{\sin^2\alpha - \sin^2\theta}{\sin 2\alpha - 2\alpha\cos 2\alpha}, \qquad (15)$$

$$u_\theta = 0,$$

where Q is the strength of the point source or point sink, and $\theta = 0$ along the axis of the wedge. Note that the radial velocity decreases uniformly as the inverse of the distance from the origin, but flow reversal does not occur. This solution may be extended to describe flow in corners with curved walls, provided a local coordinate system is used (Langlois 1964, p. 177). For a corner formed by a plane and a sinusoidal wall, the centre of the local coordinate system is located at the intersection between the plane wall and the tangent to the wavy wall. Flow reversal along the wavy wall is determined by the relative strength of the Jeffery–Hamel and the Moffatt similarity solution. When the first dominates, for small wave amplitudes, the streamlines bend to follow the curvature of the wavy wall; when the second dominates, for large wave amplitudes, flow reversal occurs.

Considering wide channels, we plot the streamline patterns for $w/\lambda = 1.000$ and 2.000 (figure 10*b*, *c*), and compare them to the corresponding ones for shear driven flow presented in figures 3(*c*) (middle panel) and 3(*d*). The comparison for $w/\lambda = 1.000$ clearly illustrates the deeper penetration of the fluid into the sinusoidal corrugations for pressure-driven flow. On the other hand, the comparison for

$w/\lambda = 2.000$ indicates a similarity in the flow structure for very wide channels. This is expected, as when w/a becomes large, the curvature of the parabolic profile in the vicinity of the wavy wall becomes less important, and the parabolic flow is locally approximated as a simple shear flow.

The incipient flow reversal curve for pressure-driven flow is shown in figure 7(*b*), along with predictions of perturbation analyses. Note the insufficiency of second-order perturbation expansion for small a/w (Appendix) to predict flow reversal. First-order perturbation expansion for small w/λ (Hasegawa & Izuchi 1983) is accurate only in a qualitative sense. At large channel widths, the separation curve tends to an asymptotic value which is identical with that for shear-driven flow, and is characteristic of simple shear flow over a sinusoidal wall. Again, an interesting interpretation arises by considering the wave amplitude constant and varying the channel width. This shows that at small amplitudes, flow reversal does not occur for any channel widths. Next, there is a range of moderate amplitudes where the flow reverses only within wide channels; the eddies produced may be suppressed by sufficiently decreasing the channel width. Finally, flow reversal always occurs for large wave amplitudes, independently of the channel width. This behaviour is fundamentally different from that for shear-driven flow, for which eddies may be produced for any wave amplitude by sufficiently decreasing the channel width.

The support of Eastman Kodak company is acknowledged.

Appendix

In this Appendix we outline a perturbation analysis of shear- and pressure-driven flow in a channel constricted by a plane wall at $y = w$, and a sinusoidal wall at $y = -a\cos(kx)$, valid for small wave amplitudes $\epsilon = a/w$. First, following Wang (1978), we introduce the stream function ψ, and expand

$$\frac{\psi}{Vw} = \psi_0 + \epsilon\psi_1 + \epsilon^2\psi_2 + \dots . \tag{A 1}$$

The zeroth-order term is equal to $\psi_0 = -\frac{1}{2}Y^2$ for Couette, and $\psi_0 = \frac{1}{6}(2Y-3)\,Y^2$ for Poiseuille flow, where $Y = y/w$. In the first case V is the velocity of the plane wall; in the second case V is defined with respect to the mean pressure gradient $G = -\mathrm{d}P/\mathrm{d}x$, as $V = Gw^2/2\mu$. In the limit of creeping motion, ψ satisfies the biharmonic equation and thus

$$\nabla^4\psi_i = 0 \quad (i = 0, 1, 2, \dots). \tag{A 2}$$

The boundary conditions satisfied by the stream function are the no-slip and no-penetration condition on the wavy and the plane wall,

$$\psi = \frac{\partial\psi}{\partial y} = 0 \quad \text{at } Y = -\epsilon\cos(kx), \tag{A 3}$$

$$\psi = 0 \quad \text{at } Y = 1,$$

and

$$-\frac{\partial\psi}{\partial y} = V \quad \text{at } Y = 1 \text{ for Couette flow},$$

or

$$\frac{\partial\psi}{\partial y} = 0 \quad \text{at } Y = 1 \text{ for Poiseuille flow}.$$

Substituting (A 1) into these equations and collecting first-order terms, we may solve for the first-order correction. Details are given by Wang (1978); the result is identical for Couette and Poiseuille flow,

$$\psi_1 = -\cos(kx)\frac{1}{R}[-2q(e^{qY}-e^{-qY})+(e^{-2q}+2q-1)\,Y\,e^{qY}+(e^{2q}-2q-1)\,Y\,e^{-qY}], \tag{A 4}$$

where $$R = e^{2q}+e^{-2q}-2-4q^2,$$

and $q = kw$. This is a purely periodic term in phase with the wave and thus, does not affect the flow rate or the mean drag force on the solid surfaces. Working in a similar fashion, we may evaluate the second-order correction (see also Munson *et al.* 1985),

$$\psi_2 = -\tfrac{1}{4}+GY-\tfrac{1}{2}GY^2+(A\,e^{2qY}+B\,e^{-2qY}+CY\,e^{2qY}+DY\,e^{-2qY})\sin(2kx), \tag{A 5}$$

where

$$A = \frac{(8q^2-e^{-4q}+1+4q-16Fq)}{4E},$$

$$B = \tfrac{1}{4}-A,$$

$$C = \frac{2q(-4q-1+e^{-4q})+4F(-1+4q+e^{-4q})}{4E},$$

$$D = \frac{2q(-4q+1-e^{4q})+4F(-1-4q+e^{4q})}{4E},$$

with

$$E = 16q^2-e^{-4q}-e^{4q}+2,$$

$$F = -\frac{q(4q+e^{-2q}-e^{2q})}{R},$$

and

$$G = F, \quad \text{for Couette flow,}$$

$$G = F-\tfrac{1}{2}, \quad \text{for Poiseuille flow.}$$

The non-periodic part of (A 5) yields an order-ϵ^2 contribution to the drag force and the flow rate. The wall shear stress may be evaluated in a straightforward fashion, by differentiating (A 1).

REFERENCES

Blake, J. R. 1971 A note on the image system for a stokeslet in a no-slip boundary. *Proc. Camb. Phil. Soc.* **70**, 303–310.

Caponi, E. A., Fornberg, B., Knight, D. D., McLean, J. W., Saffman, P. G. & Yuen, H. C. 1982 Calculations of laminar viscous flow over a moving wavy surface. *J. Fluid Mech.* **124**, 347–362.

Deiber, J. A. & Schowalter, W. R. 1979 Flow through tubes with sinusoidal axial variations in diameter. *AIChE J.* **25**, 638–645.

Fraenkel, L. E. 1962 Laminar flow in symmetrical channels with slightly curved walls. I. On the Jeffery–Hamel solutions for flow between plane walls. *Proc. Roy. Soc. Lond.* A **267**, 119–138.

Hall, P. 1974 Unsteady viscous flow in a pipe of slowly varying cross-section. *J. Fluid Mech.* **64**, 209–226.

Happel, J. & Brenner, H. 1965 *Low Reynolds Number Hydrodynamics*. Noordhoff.

Hasegawa, E. & Izuchi, H. 1983 On steady flow through a channel consisting of an uneven and a plane wall. Part 1. Case of no relative motion in two walls. *Bull. JSME* **26** (214), 514–520.

HASEGAWA, E. & IZUCHI, H. 1984 On steady flow through a channel consisting of an uneven and a plane wall. Part 2. Case of walls with a relative velocity. *Bull. JSME* **27** (230), 1631–1636.

HASIMOTO, H. & SANO, O 1980 Stokeslets and eddies in creeping flow. *Ann. Rev. Fluid Mech.* **12**, 335–363.

HIGDON, J. J. L. 1985 Stokes flow in arbitrary two-dimensional domains: shear flow over ridges and cavities. *J. Fluid Mech.* **159**, 195–226.

JEFFREY, D. J. & SHERWOOD, J. D. 1980 Streamline patterns and eddies in low-Reynolds-number flow. *J. Fluid Mech.* **96**, 315–334.

LADYZHENSKAYA, O. A. 1969 *The Mathematical Theory of Viscous Incompressible Flow.* Gordon & Breach.

LANGLOIS, W. E. 1964 *Slow Viscous Flow.* Macmillan.

LEE, S. H. & LEAL, L. G. 1986 Low-Reynolds-number flow past cylindrical bodies of arbitrary cross-sectional shape. *J. Fluid Mech.* **164**, 401–427.

MOFFATT, H. K. 1964 Viscous and resistive eddies near a sharp corner. *J. Fluid Mech.* **18**, 1–18.

MUNSON, B. R., RANGWALLA, A. A. & MANN, J. A. 1985 Low Reynolds number circular couette flow past a wavy wall. *Phys. Fluids* **28**, 2679–26.

PAN, F. & ACRIVOS, A. 1967 Steady flow in rectangular cavities. *J. Fluid Mech.* **28**, 643–655.

POZRIKIDIS, C. 1987 A study of peristaltic flows. *J. Fluid Mech.* **180**, 515–527.

SOBEY, I. J. 1980 On flow through furrowed channels. Part 1. Calculated flow patterns. *J. Fluid Mech.* **96**, 1–26.

SOBEY, I. J. 1983 The occurrence of separation in oscillatory flow. *J. Fluid Mech.* **134**, 247–257.

TAYLOR, G. I. 1971 A model for the boundary condition of a porous material. Part 1. *J. Fluid Mech.* **49**, 319–326.

WANG, C. Y. 1978 Drag due to a striated boundary in slow Couette flow. *Phys. Fluids* **21**, 697–698.